

Clear-Sky Turbulence and Shallow Convection: New Insights Combining SAR Images, Satellite Brightness Temperature and In Situ Measurements

P.-E. Brilouet¹, D. Bouniol¹, F. Couvreur¹, A. Ayet^{2,3}, C. Granero-Belinchon⁴, M. Lothon⁵ and A. Mouche⁶

¹CNRM, Université de Toulouse, Météo-France, CNRS, Toulouse, France

²CNRS, Université Grenoble Alpes, Inria, Grenoble INP, GIPSA-Lab, Grenoble, France

³CECI, Université de Toulouse, CNRS, CERFACS, Toulouse, France

⁴Mathematical and Electrical Engineering Department, IMT Atlantique, Lab-STICC, UMR CNRS 6285,

29238 Brest, France

⁵Laboratoire d'Aérodynamique, University of Toulouse, CNRS, UPS, Toulouse, France

⁶Ifremer, Univ. Brest, CNRS, IRD, Laboratoire d'Océanographie Physique et Spatiale (LOPS), IUEM,

Brest 29280, France

Key Points:

- Atmospheric coherent structures (cells, rolls and cold pools) are systematically detected and analysed in a high-resolution SAR image
- Properties of rolls from SAR measurements are comparable with the turbulence organization deduced from airborne data
- A diversity of cold pool geometrical and dynamical features is related to cloud intensity provided by satellite brightness temperature

Corresponding author: P.-E. Brilouet, pierre-etienne.brilouet@aero.obs-mip.fr

Abstract

The imprint of marine atmospheric boundary layer (MABL) dynamical structures on sea surface roughness, as seen from Sentinel-1 Synthetic Aperture Radar (SAR) acquisitions, is investigated. We focus on February 13th, 2020, a case study of the EUREC4A (Elucidating the role of clouds-circulation coupling in climate) field campaign. For clear sky conditions, convective rolls and cells imprints on sea surface roughness is confirmed through the intercomparison with MABL turbulent organization deduced from airborne measurements. A discretization of the SAR wide swath into $25 \times 25 \text{ km}^2$ tiles allows us to capture the spatial variability of the turbulence organization varying from rolls to cells. We then objectively detect cold pools within the SAR image and combine them with geostationary brightness temperature. The geometrical or physically-based metrics of cold pools are correlated to cloud properties. This provides a promising methodology to analyze the dynamics of convective systems as seen from below and above.

Plain Language Summary

We propose an innovative approach to investigate the marine atmospheric boundary layer (MABL) dynamical structures by combining spaceborne Synthetic Aperture Radar (SAR) images, brightness temperature (T_B) from the Geostationary Operational Environmental Satellite (GOES) and in situ turbulence airborne measurements from the EUREC4A field campaign. Focusing on February 13th, 2020, two types of atmospheric processes are investigated: clear sky organizations and cold pools. The signature of atmospheric coherent structures on sea surface roughness, especially convective rolls, is validated with respect to the turbulence measurements of the ATR 42 aircraft. The cold pools are detected within the SAR image using a segmentation method. Cold pool characteristics such the size and the gust front intensity can then be directly derived from the SAR image. The GOES images provide cloud field properties with the temporal dimension. Exploring backward cloud evolution with respect to the SAR image timing appears meaningful to catch the life cycle of cold pools and convective clouds from which they originate. The application of this approach could pave the way to access the dynamics of convective systems as seen from below and above, allowing to go one step further in the quantitative use of SAR images to investigate boundary layer processes.

1 Introduction

Marine atmospheric boundary layer (MABL) dynamics plays a crucial role in the mesoscale organization of convection. Among the different kinds of coherent organizations occurring inside the MABL, three-dimensional cells and quasi-two-dimensional convective rolls are frequent (Etling & Brown, 1993; Weckwerth et al., 1996; Atkinson & Wu Zhang, 1996; Wang et al., 2020). The roll wavelengths are in the range of spectral scales that contribute the most to turbulence kinetic energy (Lemone, 1976). It leads to a substantial impact on the vertical transport of heat and moisture (Chou & Ferguson, 1991; Etling & Brown, 1993; Brilouet et al., 2020), which is still not completely understood. Another important kind of MABL coherent structures are the cold pools which are key components for the life cycle of convection and cloud organization. Cold pools are generated by the downward motion of air mass cooled by rain drop evaporation. At the surface, it spreads out horizontally to form a gust front with an enhanced wind intensity. Previous studies have highlighted the relationships between cold pools, their accompanying moisture distribution and related cloud cover (Khairoutdinov & Randall, 2006; Zuidema et al., 2012; Torri et al., 2015). Cold pools can, in their core, inhibit the development of new convective cells due to their stabilizing effects. However, they can also dynamically trigger, at their edges, new convective cells, through wind convergence and lifting or thermodynamically by accumulation of moisture (Lima & Wilson, 2008; Feng et al.,

2015; Torri & Kuang, 2019). It is then fundamental to improve the monitoring of cold pools and their interplay with convection systems.

To improve understanding of MABL coherent structures, accurate measurements are needed. Most observational studies are based on in-situ data, including shipboard (e.g., Zuidema et al., 2012; de Szoeko et al., 2017) or shore-based measurements (e.g., Vogel et al., 2021): those provide thermodynamical and dynamical measurements, with however spatially-limited sampling. For shallow convection MABL coherent structures, spatial sampling could be obtained with high-resolution (< 100 m) spaceborne observations of sea-surface roughness, related to surface wind and stability variations. In particular, SAR backscatter is such a high resolution (~ 10 m – 100 m) measurement, available during day and night, regardless of weather conditions and cloud cover. Coherent structures induce a contrasts of SAR backscatter, which are however difficult to extract since they are multiscale and superimpose with other (oceanic) signatures (Kudryavtsev et al., 2005; Ayet et al., 2021). Atlas (1994) was a pioneer in highlighting the potential signature of a storm microburst on the sea surface. Further work focused on convective rolls (Alpers & Brümmer, 1994; Young et al., 2000; Vandemark et al., 2001; Wang et al., 2020), their link with stratification Stopa et al. (2022) and on deep convection cold pools from SAR winds (La et al., 2020) or from scatterometer winds (Mapes et al., 2009; Kilpatrick & Xie, 2015; Garg et al., 2020).

Systematic and quantitative extraction of high resolution information on MABL properties in SAR measurements is still a challenge, due to overlapping geophysical processes which require complementary information. The aim of this paper is thus to present an innovative approach based on a combined use of SAR and geostationary satellite data to study the interplay between the MABL and convective organization. By doing so we (i) show how SAR clear-sky convection compares to in situ measurements and (ii) analyse the morphological and dynamical properties of cold pools, related to moist convection.

The paper is organized as follows: the data and methods are presented in Section 2. Section 3 is devoted to the clear-sky turbulence and Section 4 concerns the cold pool detection and characterization. The last section concludes the paper with a discussion of the main results.

2 Data and Methods

2.1 Data

We used C-band SAR images from the Sentinel-1 satellite, which probes the sea surface through clouds, in interferometric wide swath (IW) mode. Each image is 400-km wide with effective resolution of 100 m, allowing multiscale sampling of cold pools. The C-band backscatter signal (σ_0) is sensitive to the slope distribution of centimetre-scale wind-wave, with short adjustment timescales to changes in surface wind (Kudryavtsev et al., 2005). Backscatter contrasts can thus be related to surface signatures of MABL processes (Ayet et al., 2021).

To obtain information on the cloud layer, we used infrared brightness temperature (T_B) provided by the Advanced Baseline Imager (ABI, Schmit et al., 2005) onboard GOES-16 (Geostationary Operational Environmental Satellite). In the region of interest, the Atlantic trades, cloud cover mainly consists of low-level clouds which facilitates the interpretation of the satellite images can be detected with the brightness temperature despite their small temperature differences with the sea surface. The spatial resolution is 2 km and temporal resolution 10 min.

In addition, we used wind speed and direction estimated from WindSat, a polarimetric microwave radiometer operated on the Coriolis satellite, with a spatial resolution of 25 km.

Finally, we used in situ observations from the EUREC4A campaign (Elucidating the role of clouds-circulation coupling in climate), which took place over the Western part of the Tropical Atlantic near Barbados, in Jan-Feb 2020 (Stevens et al., 2021). In particular, the SAFIRE ATR 42 aircraft samples the atmosphere around the cloud-base level and at different heights in the subcloud layer (Bony et al., 2022). Among the collected data, we will focus on the vertical velocity turbulent fluctuations (w') deduced from a five-hole radome nose with a spatial resolution of around 4 m (Brilouet et al., 2021).

Here, we focused on February 13th 2020, with the best spatial and temporal overlapping between ATR 42 and Sentinel-1 acquisition: an ATR 42 flight between 0735 UTC and 1152 UTC (take-off and landing times) and a Sentinel-1 crossing around 0935 UTC, about 100 km away from the aircraft track (see Fig. 1a). Superimposing T_B and σ_0 shows distinct atmospheric processes: clear-sky convective rolls and cold pools below clouds.

2.2 Methods

2.2.1 Characteristics from two-dimensional autocorrelation

Because turbulent processes are highly variable in time and space, as well as very sensitive to their dynamical environment, the wide swath SAR image has been split into 25×25 km² tiles (Fig. 2a). This is a good compromise with sub-domains large enough to properly sample coherent structures and small enough to be homogeneous. This is consistent with previous studies based on 20×20 km² Wave Mode SAR acquisitions which focused on convective roll analysis (Wang et al., 2019; Granero-Belinchon et al., 2022). Using the GOES image, tiles with cloudy pixels were removed from the clear-sky turbulence analysis (blue tiles in Fig. 2a). Based on in situ EUREC4A data, a T_B threshold of 292 K has been chosen : colder pixels are considered as cloudy.

Two-dimensional autocorrelation is calculated over each 25×25 km² tiled area. Following the methodology detailed in Granero-Belinchon et al. (2022), we first estimate the longitudinal axis of the coherent structures (noted hereafter as Ψ , Fig. 2b,c solid red line). Then, following Lohou et al. (2000), the integral lengthscale L_E is estimated for each angle θ and an elliptical fit is applied to the resulting polar curve (red ellipse in Figs. 2b,c). The type of organization is then diagnosed from the flatness parameter f of the ellipse. A threshold is empirically chosen to distinguish rolls ($f \geq 0.7$, green tiles in Fig. 2a and Fig. 2c) from the transition between rolls and cells ($f < 0.7$, orange tiles in Fig. 2a and Fig. 2b). When L_E anisotropy is strong enough, the orientation of the major axis provides a second estimate of the roll direction (noted hereafter as α , dashed purple line in Figs. 2b,c). Moreover, for roll tiles, the organized structure lengthscale L_{OS} is defined as the autocorrelation secondary local maximum along the direction perpendicular to the structures (blue line in Fig. 2c): it corresponds to the mean transverse lengthscale of the rolls.

2.2.2 Identification and characterization of cold pools

To analyse the morphological and dynamical characteristics of cold pool signatures on SAR, we developed an objective identification method, validated over the case study. An example a cold pool signature is given in Fig. 3a. The method makes the physical assumption that the pattern of a cold pool consists of strong positive gradients at its forward and backward edges (blue zones in Fig. 3c) and a rather smooth central area with a negative gradient (green zone in Fig. 3c). This corresponds to the gust front and to the horizontal wind divergence associated to the downdraft, respectively. The edges are first detected by computing increments on the gaussian-filtered backscatter signal and

selecting pixels with increments larger than twice the increment standard deviation. Individual cold pools objects (orange contours in Fig. 3b) are then defined by grouping edges together if a zone of negative increment exists between them (e.g., Fig. 3c, the blue edges are part of the same cold pool because of the green zone with negative increment). For the SAR image studied here, this objective methodology captures most of the cold pools, as validated visually (Fig. 4a). Future work will focus on extending this method systematically to other SAR images.

Detected cold pools were contextualized with an object identification of cloud structures within GOES T_B . The method is described in Brient et al. (2019) and Villefranche et al. (2020): it uses the watershed algorithm in space and time (3D) with two thresholds on the cloud object ($T_B \leq 292$ K) and on the cold cores ($T_B \leq 285$ K), allowing to follow the identified object in time (contours in Fig. 3e). This method thus connects the instantaneous snapshot of cold pools with the temporal evolution of the cloud organization and individual cloud life cycle.

3 Clear-Sky Turbulence

The ability of SAR to retrieve MABL turbulence activity is assessed using airborne observations. In spite of a non perfect overlap between airborne and spaceborne observations, two transects were made in the SAR image to mimic the aircraft legs (Fig. 1a). We assume the stationarity of the turbulent field and an advection with the mean wind direction of the coherent structures contained in the SAR image over the ATR 42 area. The direction of the two SAR transect (blue and green lines) was chosen to have the same orientation with respect to WindSat wind than the ATR42 (brown and orange line). The time series of w' measured by the ATR 42 and σ_0 fluctuations highlight similar signal dynamics (Fig. 1b). For the two sampling directions, signals differ significantly: the periodicity of the sampled eddies is significantly smaller for the transversal legs (blue and brown) than longitudinal ones (green and orange). This emphasizes the nonaxisymmetric behavior of both turbulence and roughness fields.

To document the uncertainties associated to the unidirectional nature of the in situ airborne sampling, a set of 40 1D-SAR transects is extracted (contained within the pink parallelepiped in Fig. 1a). The L_{OS} computed on this set show a substantial variability between 1.10 km and 4.71 km with an average value of 2.65 km (see the boxplot in Fig. 1f). The estimates made on the ATR legs at 300 m and 600 m are 1.60 km and 2.00 km, respectively, are well within this range of values covered by the 1D-SAR estimates. This result is in line with the study of Vandemark et al. (2001) and consolidates the hypothesis of a sea surface roughness imprint from MABL coherent structures. One of the SAR strength is to provide a 2D-field of roughness which allows for 2D autocorrelation analysis. In the present case, the estimate of L_{OS} over the pink area from the 2D autocorrelation, 2.90 km, is well consistent with the 1D SAR range of values and with in situ estimates. In the SAR subdomain considered here, a dropsonde launched from the HALO aircraft close to the SAR passage timing reveals a well-mixed MABL with a depth of $z_i = 570$ m. It leads to an aspect ratio of 5.1. For ATR42 measurements, the MABL depth estimates are variable, ranging from $z_i = 500$ m to $z_i = 800$ m. This variability can be driven by dry air intrusions from the troposphere or by secondary circulation dynamics generated by the mesoscale cloud system. Therefore, the aspect ratio estimates in the ATR42 flight area are ranging from 2 to 4. The aspect ratio is commonly between 2 to 6, with some observed extreme values higher than 10 (LeMone, 1973; Brown, 1980; Etling & Brown, 1993). One of the common MABL parameter extracted from SAR measurements is its depth, assuming a fixed aspect ratio (Sikora et al., 1997; Young et al., 2000). We advise caution when using this estimation method given the spread in observed aspect ratios and the spatial variability of MABL depths.

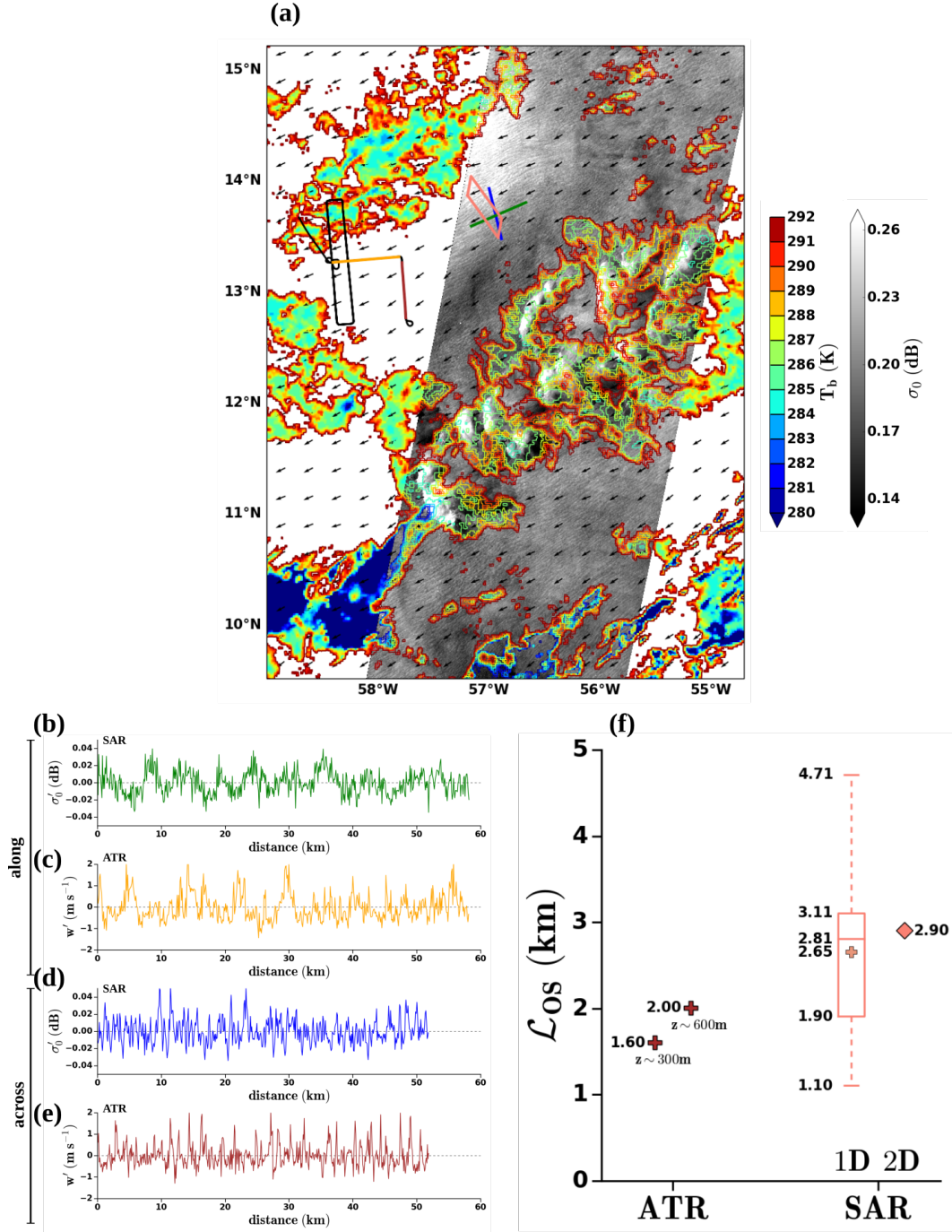


Figure 1. (a) Backscatter signal from SAR (σ_0), superimposed with the infrared brightness temperature from GOES and wind vector from WindSat for February 13, 2020. Time series of (b) and (c) along-wind σ_0 fluctuations in green and ATR 42 vertical velocity fluctuations (w') at $z \sim 300$ m in orange, (d) and (e) cross-wind σ_0 in blue and w' in brown. The aircraft and SAR transects are shown by the different colored lines in map (a). (f) Organized structure length-scale (L_{os}) estimates from the ATR 42, from SAR with 1D and 2D autocorrelations in the pink diamond area.

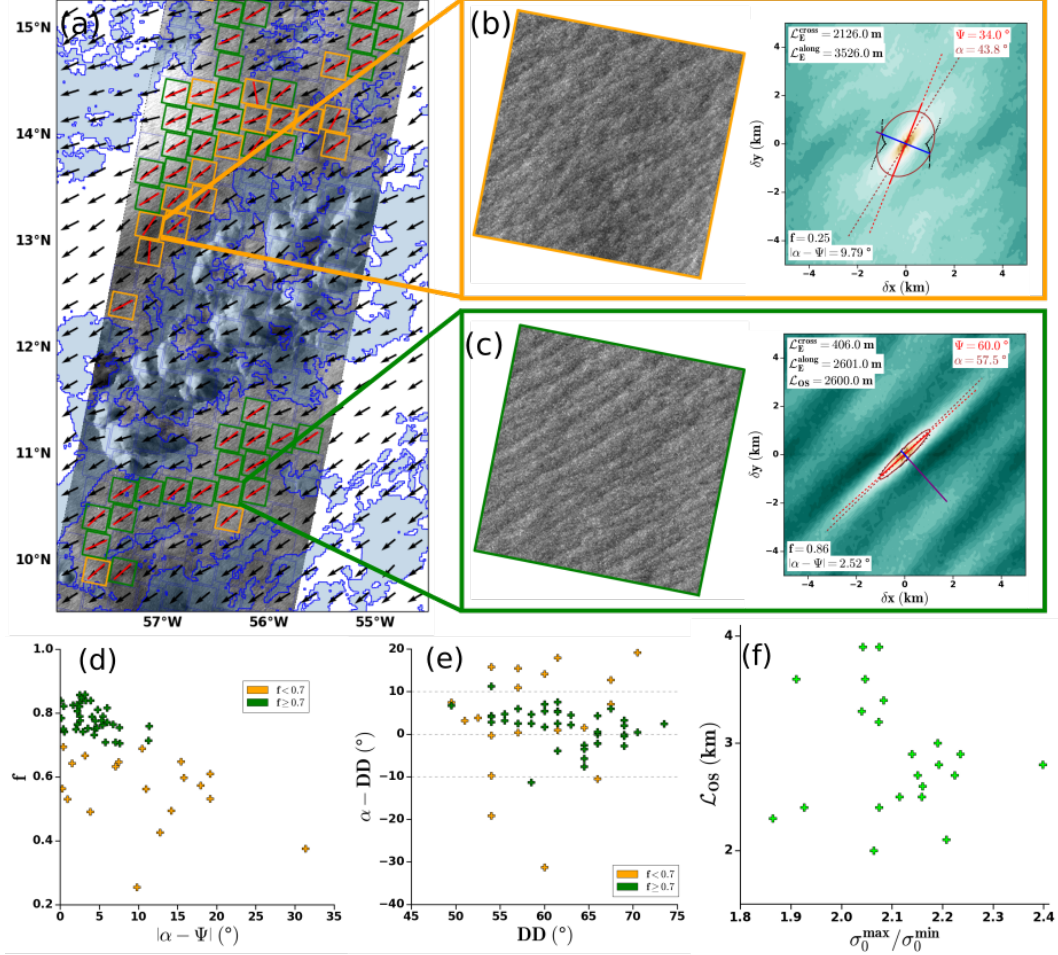


Figure 2. (a) SAR image with an organization criterion: cell / roll transitions ($f < 0.7$) in orange and rolls ($f \geq 0.7$) in green. The black arrows are the WindSat wind and the red lines are the roll directions. Examples of σ_0 and associated 2D autocorrelation for (b) a cell / roll transition regime and (c) a well-established rolls regime. (d) Flatness versus the difference between the two estimates of structure directions, (e) difference between the structure direction and the wind direction and (f) organized structure lengthscale (L_{OS}) according to the ratio $\max(\sigma_0) / \min(\sigma_0)$ over each tiles.

The 2D autocorrelation analysis, extended to 58 subdomains in the entire SAR image (Fig. 2a), allows us to explore the spatial variability of MABL structures. The separation between cells and transition zones using the flatness criterion shows that convective rolls (green tiles) are the dominant type of clear sky MABL organization, given the prevailing large-scale conditions of strong wind speed (Etling & Brown, 1993). Also, the transition zones (orange tiles) are mainly located downwind of cloud boundaries. They can be interpreted as buffer zones between the sub-cloud organization driven by the cold pools and the clear-sky rolls, only slightly disturbed by the cloud activity.

When the occurring structures are clearly identified as convective rolls, the difference between the two independent estimates of roll orientation, Ψ and α , becomes low (Fig. 2d). The roll direction estimate is hence robust, unlike cell/roll transition cases for which defining a direction is hardly relevant. Over the study area, the wind direction from WindSat, exhibits only slight variations, between 50° and 75° , characteristic of the established trade-wind flow. The roll axis is mostly oriented along the mean MABL wind, with a slight positive bias and a variability that can reach $\pm 10^\circ$ (Fig. 2e), in line with previous studies (Alpers & Brümmer, 1994; Atkinson & Wu Zhang, 1996; Wang et al., 2019). Over the 39 tiled areas detected as rolls, 22 have a well-marked periodicity scale (\mathcal{L}_{OS}), while others do not have a noticeable periodicity but are still stretched structures along the mean wind direction. In order to evaluate the roll size evolution as a function of the dynamic conditions, \mathcal{L}_{OS} as a function of the ratio between the maximum and the minimum of σ_0 over a each tile is shown in Fig. 2f. We assume that a higher modulation of the roughness is associated to stronger roll imprints: which is confirmed by the results of Fig. 2f.

The WindSat wind speed estimates have low variability, with values between 10.0 m s^{-1} and 11.0 m s^{-1} and an accuracy of 0.2 m s^{-1} (Zhang et al., 2018). Even if the wind speed is almost constant, the roll sizes are variable. Convective rolls are preferentially encountered when shear-induced turbulence dominates (Etling & Brown, 1993; Stopa et al., 2022). As the shear is proportional to the cube of the surface velocity, the wind intensity is a key parameter in the development of these coherent structures but it is not the exclusive source of roll size variability. Based only on one case study, these results should be considered with caution. Such analysis should be applied on all the SAR wide swath images available during the EUREC4A field campaign to document the diversity of large-scale conditions.

4 Shallow Convection and Cold Pools

Figure 3b illustrates the results of the cold pool identification method on an isolated feature in the south of the SAR swath. From the detected contours of the cold pool (orange lines), an ellipse can be fitted (green circle), and morphological characteristics of the detected feature can be derived, such as the size, the center of gravity, the flatness and the orientation of the ellipse. Also, dynamic properties can be inferred such as the intensity of the gust front gradient (Fig. 3c), equal to $4.09 \times 10^{-2} \text{ dB km}^{-1}$ which can be indicative of an active cold pool or the maximum of roughness (yellow contour in Fig. 3a), equal to $4.16 \times 10^{-1} \text{ dB}$. In SAR observations, the origin of such strong localized σ_0 increase can be ambiguous between a rain signature (Alpers et al., 2016) or a disturbance of the signal due to the hydrometeors in the upper part of a deep convective system (Alpers et al., 2021). Only shallow convective clouds were encountered during EUREC4A, with cloud top around 2 km - 3 km and no ice hydrometeors are present. Therefore, such roughness peaks is related to a splash zone, associated with rain cells.

The superposition of GOES T_B on SAR σ_0 at the same time (Fig. 3d) highlights the strong correlation between the cold pool imprint on the sea surface roughness and the cloud organization. Cloud and MABL dynamic processes are tightly coupled, with shallow convective clouds that remain mainly connected to the MABL. Based on the anal-

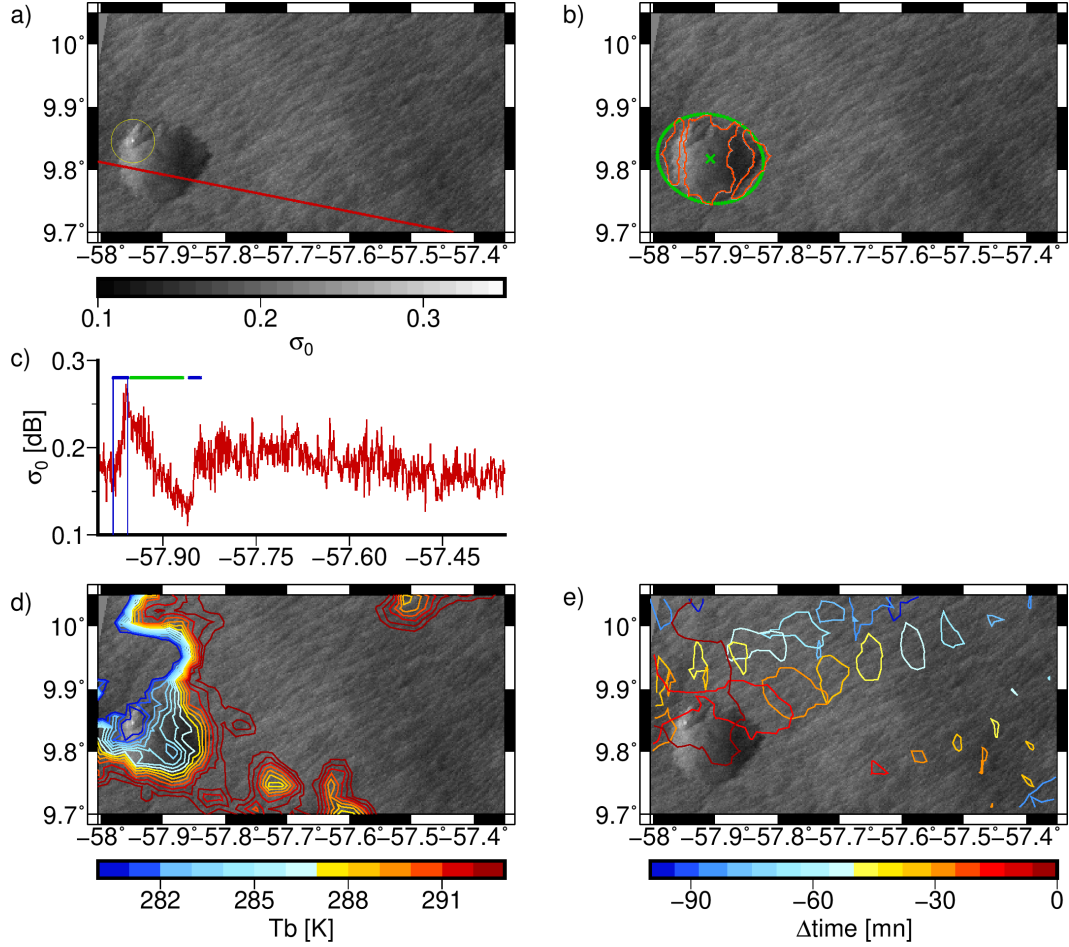


Figure 3. Identification method applied on an isolated cold pool and associated metrics. (a) Backscatter signal centered on the studied feature. (b) Results of the detection method (pink contours) and elliptical fit (green contours). (c) Transect across the cold pool along the red line shown in (a). (d) Brightness temperature superimposed on the SAR image at the same instant. (e) Backward tracking of the cloud cold core ($T_B \leq 285$ K).

ysis of the synoptic conditions, the large patch of T_B colder than 280 K in the northwest of the cold pool, is due to high clouds with a north eastward advection typical of the atmospheric layer above the south westward trade wind flow. There is no apparent signature on the surface, these high clouds are completely decoupled of the MABL. However, a relative minimum in T_B that can be associated to an ascending core can be observed above the cold pool. In addition to the collocated SAR – GOES superposition in time, a tracking of the cloud cold core ($T_B \leq 285$ K) is performed, as shown in Fig. 3e. At the SAR timing, the high altitude cloud layer interferes with the shallow convection clouds but the distinction is noticeable as soon as we go back 5 min before. The progressive growth of the cloud from its origin is observed. The 285 K level for this cloud was first detected at 0810 UTC at about 61 km with a growth factor of $1.4 \text{ km}^2 \text{ min}^{-1}$ during the first hour following its detection. This backward tracking allows to explore the origin of the cloud entity and provides an estimate of the cold pool lifetime up to the present time, which in this case is about 1 hour.

The application of the identification method on the entire large swath leads to the detection of 68 cold pools (Fig. 4a). Most of them are located below the mesoscale shallow clouds in the center of the image. Due to interactions and collisions between them, these cold pools present a wide variability of size, shape and orientation. Some cold pools, associated with isolated clouds, have a smaller variability of geometric parameters and are generally smaller than the aggregated cold pools. The deduced morphological and dynamic cold pool metrics allow us to explore the physical processes involved. In particular, a correlation between the area of the cold pool and the maximum of σ_0 over the cold pool is found (Fig. 4b). The more active and more precipitating clouds continue to energetically supply the cold pool through rain evaporation, which leads to a spreading of the latter. Furthermore, these convective systems induce a high σ_0 maximum either related to splash zones directly due to the rain or to an increase of the wind intensity thanks to secondary circulations. The more active cold pools have a stronger roughness contrast (maximum of σ_0) with their environment and thus a sharper edge gradient related to the gust front gradient intensity (Fig. 4e).

Cloud properties can be inferred from T_B and put in relation with cold pool properties from SAR measurements. The parameter $\Delta_{\text{lfe}}T_B$ is the difference between the minimum of T_B at the present time and the one since the first detection of the 285 K level, over the followed cloud object. If $\Delta_{\text{lfe}}T_B$ is equal to 0, the T_B minimum is reached at the SAR timing, and the higher $\Delta_{\text{lfe}}T_B$, the older the cloud peak intensity. A tendency emerges, with less intense cold pool gust front gradients for higher $\Delta_{\text{lfe}}T_B$ (Fig. 4c). This reflects a coupled loss of convective intensity both in the cloud layer and at the surface, with potentially dissipating cold pools. The parameter $\Delta_{\text{shield}}T_B$ is defined, at each instant, as the difference between the averaged T_B of the cloud and the minimum of T_B for this cloud. It provides insight into how active the cloud is, a small $\Delta_{\text{shield}}T_B$ indicates the existence of cold cores and localized vertical developments. Higher σ_0 maxima are associated to smaller $\Delta_{\text{shield}}T_B$ (Fig. 4d), which allow us to connect the more intense cold pool imprint seen from below, at the surface to the intensity of the convective activity seen from above.

5 Conclusions

Based on an EUREC4A case study, an extensive analysis of a wide swath SAR image has been performed with the combined use of in situ airborne measurement and geostationary brightness temperature. The SAR backscattered signal provides a quasi-instantaneous picture of the sea surface roughness. The signatures of clear-sky organization into convective rolls and cold pools below clouds have been analyzed.

The intercomparison of the observed structures on the sea surface roughness with the MABL turbulent organization through the vertical velocity fluctuations measured by the ATR 42 aircraft has allowed to consolidate the hypothesis of a significant relationship between the surface small scales and the MABL processes. The SAR wide swath has been divided into sub-domains of $25 \times 25 \text{ km}^2$ to perform, on clear-sky areas, 2-D autocorrelation of the high resolution roughness, enabling us to capture the spatial variability MABL organization. Considering the observed high wind speed conditions, the convective rolls were the predominant coherent structures. These rolls are almost oriented in the mean surface wind direction with characteristic scales between 2.0 and 3.9 km. The cell/roll transition zones have been mainly observed in the surrounding clear-sky environment of clouds.

Shallow convective systems have been investigated with an innovative approach, combining the SAR σ_0 with the geostationary cloud T_B in order to access the dynamics of clouds as seen from below and above. A segmentation method has been developed to detect the cold pools on σ_0 . The characteristics of the cold pools, based on geometrical or physically-based metrics are thus extracted. Within the SAR wide swath, a large

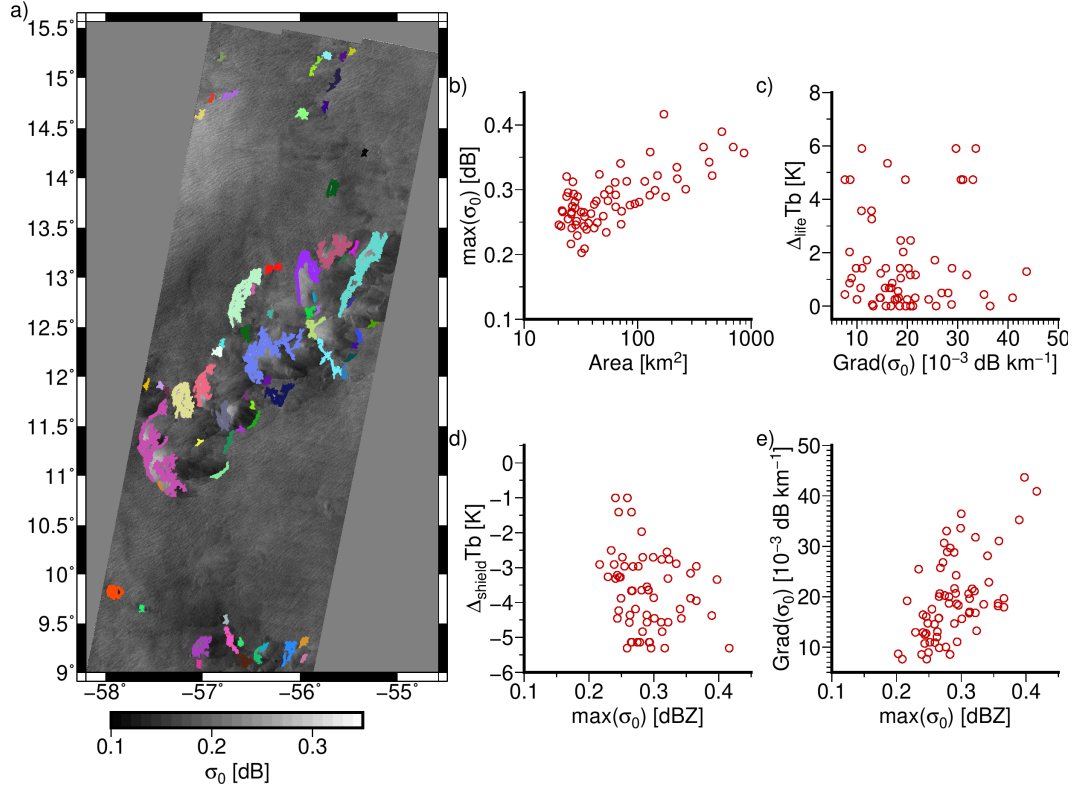


Figure 4. (a) Overview of the cold pool detection over the entire large swath, (b) σ_0 maximum versus the area, (c) $\Delta_{\text{life}} T_B$ versus the gust front gradient, (d) $\Delta_{\text{shield}} T_B$ versus the σ_0 maximum and (e) gust front gradient versus σ_0 maximum.

number of cold pools have been identified with significant variability in their properties. The more active cold pools, associated with a higher MABL dynamic intensity, present sharper edge roughness contrasts and higher roughness maxima. The intensity of the cloud activity, with a pronounced vertical development, has been connected to the strong cold pool imprint on sea surface roughness. Also, the relation between the decrease of convective intensity in the cloud layer and the dissipating cold pools at the surface has been noted.

The new perspectives, presented here with a case study, on clear-sky turbulence and shallow convection which can be extracted from a wide swath SAR image can pave the way to improve our understanding of boundary layer processes from satellite observations. The opportunity to jointly analyze characteristics of cold pools and related convection cloud organization, which can take a spectacular variety of forms and shapes (such as isolated clouds, arcs, mesoscale systems, ...) should provide significant insights into the mechanisms involved. The next step is to apply our approach to an ensemble of varying conditions, targeting other regions and convective regimes, both shallow and deep convection. The surrounding clear-sky environment and its interplay with the cloud systems are also of great interest.

6 Open Research

Sentinel-1 is part of the European space component of the Copernicus European program. level-1 GRD data are free of charge and available on the Copernicus Open Access Hub (<https://sentinels.copernicus.eu/web/sentinel/sentinel-data-access>). GOES-16 ABI Level 1b radiances are available at <https://doi.org/10.7289/V5BV7DSR>. WindSat data are produced by Remote Sensing Systems and sponsored by the NASA Earth Science MEaSUREs DISCOVER Project and the NASA Earth Science Physical Oceanography Program. RSS WindSat data are available at <https://data.remss.com/windsat/>. The EUREC4A turbulence dataset derived from the SAFIRE ATR 42 aircraft is available on the AERIS database (<https://doi.org/10.25326/128>).

Acknowledgments

The EUREC4A project provided a relevant framework for this study. PEB and AA were supported through a Postdoctoral Grant funded by the Centre National d'Études Spatiales (CNES). Airborne data were obtained from the ATR aircraft operated by SAFIRE, the French facility for airborne research, an infrastructure of the CNRS, Météo-France and the CNES. AM was supported by the ESA Sentinel-1 Mission Performance Center (4000107360/12/I-LG). We also thanks the CNES which provide, through the TOSCA PROCONUM project (Pi. DB) the facilities for authors to collaborate.

References

- Alpers, W., & Brümmer, B. (1994). Atmospheric boundary layer rolls observed by the synthetic aperture radar aboard the ers-1 satellite. *Journal of Geophysical Research: Oceans*, 99(C6), 12613-12621. doi: <https://doi.org/10.1029/94JC00421>
- Alpers, W., Zhang, B., Mouche, A., Zeng, K., & Chan, P. W. (2016). Rain footprints on c-band synthetic aperture radar images of the ocean - revisited. *Remote Sensing of Environment*, 187, 169-185. doi: <https://doi.org/10.1016/j.rse.2016.10.015>
- Alpers, W., Zhao, Y., Mouche, A. A., & Chan, P. W. (2021). A note on radar signatures of hydrometeors in the melting layer as inferred from sentinel-1 sar data acquired over the ocean. *Remote Sensing of Environment*, 253, 112177. doi: <https://doi.org/10.1016/j.rse.2020.112177>

- Atkinson, B. W., & Wu Zhang, J. (1996). Mesoscale shallow convection in the atmosphere. *Reviews of Geophysics*, 34(4), 403-431. doi: <https://doi.org/10.1029/96RG02623>
- Atlas, D. (1994). Footprints of storms on the sea: A view from spaceborne synthetic aperture radar. *Journal of Geophysical Research: Oceans*, 99(C4), 7961-7969. doi: <https://doi.org/10.1029/94JC00250>
- Ayet, A., Rascle, N., Chapron, B., Couvreur, F., & Terray, L. (2021). Uncovering air-sea interaction in oceanic submesoscale frontal regions using high-resolution satellite observations. *US Clivar variations*, 19(1). doi: <https://doi.org/10.5065/ybca-0s03>
- Bony, S., Lothon, M., Delanoë, J., Coutris, P., Etienne, J.-C., Aemisegger, F., ... Vogel, R. (2022). EUREC⁴A observations from the SAFIRE ATR42 aircraft. *Earth System Science Data Discussions*, 2022, 1-61. doi: [10.5194/essd-2021-459](https://doi.org/10.5194/essd-2021-459)
- Brient, F., Couvreur, F., Villefranque, N., Rio, C., & Honnert, R. (2019, March). Object-Oriented Identification of Coherent Structures in Large Eddy Simulations: Importance of Downdrafts in Stratocumulus. *Geophysical Research Letters*, 46(5), 2854-2864. doi: <https://doi.org/10.1029/2018GL081499>
- Brilouet, P.-E., Durand, P., Canut, G., & Fourrié, N. (2020). Organized turbulence in a cold-air outbreak: Evaluating a large-eddy simulation with respect to airborne measurements. *Boundary-Layer Meteorology*, 175(1), 57-91. doi: <https://doi.org/10.1007/s10546-019-00499-4>
- Brilouet, P.-E., Lothon, M., Etienne, J.-C., Richard, P., Bony, S., Lernoult, J., ... Charoy, T. (2021). The EUREC⁴A turbulence dataset derived from the SAFIRE ATR 42 aircraft. *Earth System Science Data Discussions*, 2021, 1-28. doi: [10.5194/essd-2021-52](https://doi.org/10.5194/essd-2021-52)
- Brown, R. A. (1980). Longitudinal instabilities and secondary flows in the planetary boundary layer: A review. *Reviews of Geophysics*, 18(3), 683-697. doi: <https://doi.org/10.1029/RG018i003p00683>
- Chou, S.-H., & Ferguson, M. P. (1991). Heat fluxes and roll circulations over the western gulf stream during an intense cold-air outbreak. *Boundary-layer meteorology*, 55(3), 255-281. doi: <https://doi.org/10.1007/BF00122580>
- de Szoeki, S. P., Skillingstad, E. D., Zuidema, P., & Chandra, A. S. (2017). Cold pools and their influence on the tropical marine boundary layer. *Journal of the Atmospheric Sciences*, 74(4), 1149 - 1168. doi: <https://doi.org/10.1175/JAS-D-16-0264.1>
- Etling, D., & Brown, R. A. (1993). Roll vortices in the planetary boundary layer: A review. *Boundary-Layer Meteorology*, 65(3), 215-248. doi: <https://doi.org/10.1007/BF00705527>
- Feng, Z., Hagos, S., Rowe, A. K., Burleyson, C. D., Martini, M. N., & de Szoeki, S. P. (2015). Mechanisms of convective cloud organization by cold pools over tropical warm ocean during the amie/dynamo field campaign. *Journal of Advances in Modeling Earth Systems*, 7(2), 357-381. doi: <https://doi.org/10.1002/2014MS000384>
- Garg, P., Nesbitt, S. W., Lang, T. J., Priftis, G., Chronis, T., Thayer, J. D., & Hence, D. A. (2020). Identifying and characterizing tropical oceanic mesoscale cold pools using spaceborne scatterometer winds. *Journal of Geophysical Research: Atmospheres*, 125(5), e2019JD031812. doi: <https://doi.org/10.1029/2019JD031812>
- Granero-Belinchon, C., Roux, S., Garnier, N., Tandeo, P., Chapron, B., & Mouche, A. (2022). Two-dimensional structure functions to characterize convective rolls in the marine atmospheric boundary layer from sentinel-1 SAR images. doi: <https://hal.archives-ouvertes.fr/hal-03576400>
- Khairoutdinov, M., & Randall, D. (2006). High-resolution simulation of shallow-to-deep convection transition over land. *Journal of the Atmospheric Sciences*,

- 63(12), 3421 - 3436. doi: <https://doi.org/10.1175/JAS3810.1>
- Kilpatrick, T. J., & Xie, S.-P. (2015). Ascet observations of downdrafts from mesoscale convective systems. *Geophysical Research Letters*, 42(6), 1951-1958. Retrieved from <https://agupubs.onlinelibrary.wiley.com/doi/abs/10.1002/2015GL063025> doi: <https://doi.org/10.1002/2015GL063025>
- Kudryavtsev, V., Akimov, D., Johannessen, J., & Chapron, B. (2005). On radar imaging of current features: 1. model and comparison with observations. *Journal of Geophysical Research: Oceans*, 110(C7). doi: <https://doi.org/10.1029/2004JC002505>
- La, T. V., Messenger, C., Honnorat, M., Sahl, R., Khenchaf, A., Channelliere, C., & Lattes, P. (2020). Use of sentinel-1 c-band sar images for convective system surface wind pattern detection. *Journal of Applied Meteorology and Climatology*, 59(8), 1321 - 1332. doi: <https://doi.org/10.1175/JAMC-D-20-0008.1>
- LeMone, M. A. (1973). The structure and dynamics of horizontal roll vortices in the planetary boundary layer. *Journal of Atmospheric Sciences*, 30(6), 1077 - 1091. doi: [https://doi.org/10.1175/1520-0469\(1973\)030<1077:TSADOH>2.0.CO;2](https://doi.org/10.1175/1520-0469(1973)030<1077:TSADOH>2.0.CO;2)
- Lemone, M. A. (1976). Modulation of turbulence energy by longitudinal rolls in an unstable planetary boundary layer. *Journal of Atmospheric Sciences*, 33(7), 1308 - 1320. doi: [https://doi.org/10.1175/1520-0469\(1976\)033<1308:MOTEBL>2.0.CO;2](https://doi.org/10.1175/1520-0469(1976)033<1308:MOTEBL>2.0.CO;2)
- Lima, M. A., & Wilson, J. W. (2008). Convective storm initiation in a moist tropical environment. *Monthly Weather Review*, 136(6), 1847 - 1864. doi: <https://doi.org/10.1175/2007MWR2279.1>
- Lohou, F., Druilhet, A., Campistron, B., Redelspergers, J.-L., & Saïd, F. (2000). Numerical study of the impact of coherent structures on vertical transfers in the atmospheric boundary layer. *Boundary-layer meteorology*, 97(3), 361-383. doi: [10.1023/A:1002641728075](https://doi.org/10.1023/A:1002641728075)
- Mapes, B., Milliff, R., & Morzel, J. (2009). Composite life cycle of maritime tropical mesoscale convective systems in scatterometer and microwave satellite observations. *Journal of the Atmospheric Sciences*, 66(1), 199 - 208. doi: <https://doi.org/10.1175/2008JAS2746.1>
- Schmit, T. J., Gunshor, M. M., Menzel, W. P., Gurka, J. J., Li, J., & Bachmeier, A. S. (2005). Introducing the next-generation advanced baseline imager on goes-r. *Bulletin of the American Meteorological Society*, 86(8), 1079 - 1096. doi: <https://doi.org/10.1175/BAMS-86-8-1079>
- Sikora, T. D., Young, G. S., Shirer, H. N., & Chapman, R. D. (1997). Estimating convective atmospheric boundary layer depth from microwave radar imagery of the sea surface. *Journal of Applied Meteorology*, 36(7), 833 - 845. doi: [https://doi.org/10.1175/1520-0450\(1997\)036<0833:ECABLD>2.0.CO;2](https://doi.org/10.1175/1520-0450(1997)036<0833:ECABLD>2.0.CO;2)
- Stevens, B., Bony, S., Farrell, D., Ament, F., Blyth, A., Fairall, C., ... Zöger, M. (2021). EUREC⁴A. *Earth System Science Data Discussions*, 2021, 1-78. doi: [10.5194/essd-2021-18](https://doi.org/10.5194/essd-2021-18)
- Stopa, J. E., Wang, C., Vandemark, D., Foster, R., Mouche, A., & Chapron, B. (2022). Automated global classification of surface layer stratification using high-resolution sea surface roughness measurements by satellite synthetic aperture radar. *Geophysical Research Letters*, 49(12), e2022GL098686. doi: <https://doi.org/10.1029/2022GL098686>
- Torri, G., & Kuang, Z. (2019). On cold pool collisions in tropical boundary layers. *Geophysical Research Letters*, 46(1), 399-407. doi: <https://doi.org/10.1029/2018GL080501>
- Torri, G., Kuang, Z., & Tian, Y. (2015). Mechanisms for convection triggering by cold pools. *Geophysical Research Letters*, 42(6), 1943-1950. doi: <https://doi.org/10.1002/2015GL063227>

- Vandemark, D., Mourad, P. D., Bailey, S. A., Crawford, T. L., Vogel, C. A., Sun, J., & Chapron, B. (2001). Measured changes in ocean surface roughness due to atmospheric boundary layer rolls. *Journal of Geophysical Research: Oceans*, 106(C3), 4639-4654. doi: <https://doi.org/10.1029/1999JC000051>
- Villefranche, N., Williamson, D., Couvreur, F., Hourdin, F., Gautrais, J., Fournier, R., ... Volodina, V. (2020). Process-based climate model development harnessing machine learning: Iii. the representation of cumulus geometry and their 3d radiative effects. *Earth and Space Science Open Archive*, 30. doi: <https://doi.org/10.1002/essoar.10505088.1>
- Vogel, R., Konow, H., Schulz, H., & Zuidema, P. (2021). A climatology of trade-wind cumulus cold pools and their link to mesoscale cloud organization. *Atmospheric Chemistry and Physics*, 21(21), 16609-16630. doi: <https://doi.org/10.5194/acp-21-16609-2021>
- Wang, C., Mouche, A., Foster, R. C., Vandemark, D. C., Stopa, J. E., Tandeo, P., ... Chapron, B. (2019). Characteristics of Marine Atmospheric Boundary Layer Roll Vortices from Sentinel-1 Sar Wave Mode. *IGARSS 2019 - 2019 IEEE International Geoscience and Remote Sensing Symposium*, 7908-7911. doi: <https://doi.org/10.1109/IGARSS.2019.8900287>
- Wang, C., Vandemark, D., Mouche, A., Chapron, B., Li, H., & Foster, R. C. (2020). An assessment of marine atmospheric boundary layer roll detection using sentinel-1 sar data. *Remote Sensing of Environment*, 250, 112031. doi: <https://doi.org/10.1016/j.rse.2020.112031>
- Weckwerth, T. M., Wilson, J. W., & Wakimoto, R. M. (1996). Thermodynamic variability within the convective boundary layer due to horizontal convective rolls. *Monthly Weather Review*, 124(5), 769 - 784. doi: [https://doi.org/10.1175/1520-0493\(1996\)124<0769:TVWTCB>2.0.CO;2](https://doi.org/10.1175/1520-0493(1996)124<0769:TVWTCB>2.0.CO;2)
- Young, G. S., Sikora, T. D., & Winstead, N. S. (2000). Inferring marine atmospheric boundary layer properties from spectral characteristics of satellite-borne sar imagery. *Monthly Weather Review*, 128(5), 1506 - 1520. doi: [https://doi.org/10.1175/1520-0493\(2000\)128<1506:IMABLP>2.0.CO;2](https://doi.org/10.1175/1520-0493(2000)128<1506:IMABLP>2.0.CO;2)
- Zhang, L., Shi, H., Wang, Z., Yu, H., Yin, X., & Liao, Q. (2018). Comparison of wind speeds from spaceborne microwave radiometers with in situ observations and ecmwf data over the global ocean. *Remote Sensing*, 10(3). doi: <https://doi.org/10.3390/rs10030425>
- Zuidema, P., Li, Z., Hill, R. J., Bariteau, L., Rilling, B., Fairall, C., ... Hare, J. (2012). On trade wind cumulus cold pools. *Journal of the Atmospheric Sciences*, 69(1), 258 - 280. doi: <https://doi.org/10.1175/JAS-D-11-0143.1>